

Copy
RM L57D25a

NACA RM L57D25a

23p

N 63 16238

code-1



Classification Changed to
Classified Effective 18 April 1963
Authority NASA COM-3 By J.J. Carroll

RESEARCH MEMORANDUM

FACTORS AFFECTING LOADS AT HYPERSONIC SPEEDS

By Arthur Henderson, Jr., and Mitchel H. Bertram

Langley Aeronautical Laboratory
Langley Field, Va.

OTS PRICE

EROX	\$	<u>2.60</u>
MICROFILM	\$	<u>0.89</u>

CLASSIFIED DOCUMENT

This material contains information affecting the National Defense of the United States within the meaning of the espionage laws, Title 18, U.S.C., Secs. 793 and 794, the transmission or revelation of which in any manner to an unauthorized person is prohibited by law.

NATIONAL ADVISORY COMMITTEE FOR AERONAUTICS

WASHINGTON

June 19, 1957



NATIONAL ADVISORY COMMITTEE FOR AERONAUTICS

RESEARCH MEMORANDUM

FACTORS AFFECTING LOADS AT HYPERSONIC SPEEDS

By Arthur Henderson, Jr., and Mitchel H. Bertram

SUMMARY

16238

This paper gives a brief summary of current loads information at hypersonic speeds. Several methods which the designer can employ in estimating the loads on various aircraft components are discussed. The paper deals with the characteristics of both slender and blunt configurations and touches upon the effects of boundary-layer and aerodynamic interference.

INTRODUCTION

The calculation of loads at hypersonic speeds requires the use of techniques with which many designers are not very familiar. The methods based on linear or second-order theory, which were widely used at supersonic speeds, are inadequate for slender configurations at hypersonic speeds and, of course, are completely inapplicable to configurations with blunt noses or leading edges.

In this paper it is shown that certain simplifying features which allow good design approximations of loads to be made with a minimum of effort exist at hypersonic speeds. In addition, some of the unsolved problems associated with hypersonic phenomena are pointed out.

SYMBOLS

- a speed of sound
- A constant
- c local chord length
- \bar{c} mean aerodynamic chord
- c_n section normal-force coefficient





C_p	local surface pressure coefficient
d	maximum body diameter
h	height of wedge
K	hypersonic similarity parameter, $M \frac{d}{l}$
l	length of nose or wedge
M	Mach number
p	pressure
r	radius
R	Reynolds number
s	arc length
t	thickness
V	velocity
x	distance from nose or leading edge in body-axis system
α	angle of attack
γ	ratio of specific heats
δ	flap deflection angle
Δ	incremental value
ϵ	distance between adjacent streamlines
θ	cone shock angle
Λ	sweepback angle
σ	cone semiapex angle
τ	time
φ	meridian angle



Subscripts:

∞	free-stream conditions
B(W)	body in presence of wing
MAX	maximum
s	shoulder
t	based on thickness
d	based on diameter

DISCUSSION

There are several methods which the designer can employ in arriving at an estimate of the loads on the various aircraft components. Before discussing them, however, it is instructive to consider, qualitatively, how hypersonic phenomena differ from supersonic.

Although hypersonic flow introduces many problems which were not encountered at supersonic speeds, it also introduces certain simplifying features; and aerodynamicists have not been long in taking advantage of them. For example, one source of simplification at hypersonic speeds is the fact that, in the exact shock equations, the Mach number term is usually squared and often appears in the denominator. Thus, as the Mach number increases, these terms become insignificant; thus relatively simple expressions often yield accurate approximations for certain flow properties at hypersonic speeds.

Slender Configurations

Characteristics of hypersonic flow.- Some simplifying features of hypersonic flow are illustrated in figures 1 and 2. One of the characteristics of hypersonic flow is its tendency toward two-dimensionality when in contact with slender bodies or surfaces. (See fig. 1.) The upper half of figure 1 depicts a sharp-leading-edge sweptback wing in a low and in a high Mach number flow field. There are two streamlines the same distance ϵ apart. As shown by the dashed lines, the fields of influence from each disturbance point along the leading edge spread across the wing in supersonic flow, whereas they are confined to a relatively narrow region in hypersonic flow. In addition, the right streamline of each pair will strike the leading edge later than the left one, the time lag being $\Delta\tau = \frac{\epsilon \tan \Lambda}{Ma}$. Obviously, as the Mach number increases, the time



lag decreases; thus at high Mach numbers the right streamline strikes the leading edge at almost the same time as the left one. Consequently, as far as the fluid itself is concerned, it feels as though it is practically two dimensional.

The bottom half of figure 1 depicts the fundamental basis of the generalized shock-expansion method as applied to slender three-dimensional bodies. As Eggers and Savin (ref. 1) have shown, so long as the divergence of streamlines along the body is negligible, the flow on the body surface and the associated flow field will be essentially two-dimensional in nature; consequently, two-dimensional shock-expansion theory can be used to analyze the flow about slender bodies of revolution.

Hypersonic similarity law.- The designer has another powerful tool at his disposal in the form of the hypersonic similarity law (see, for example, refs 2 to 4), which states that the pressures at corresponding points on similarly shaped bodies are identical if, for the two bodies, the product of free-stream Mach number and thickness ratio is a constant.

The physical concept behind the hypersonic similarity law is illustrated qualitatively in figure 2. Two marbles are shown, each rolling toward its own wedge. The upper marble will rise a height h in the length l_1 with the velocity V_1 , while the lower marble will rise the same height h in the longer length $l_2 = A l_1$ but with the higher velocity $V_2 = A V_1$. The ratio of lengths and velocities is such that both marbles rise the same height h in the same length of time; that is, they both experience the same change of velocity and, consequently, each marble will impart the same amount of momentum to its particular wedge. If the marbles are thought of as air molecules and the wedges as corresponding slopes on two similar bodies, a direct analogy with the hypersonic similarity law is immediately apparent.

The approximate region in which the hypersonic similarity law is applicable has been determined by Lees (ref. 5) to be about as shown in figure 3 for cones. This region is determined by the condition that the cone shock angle θ_s is less than 24° . Thus, the maximum cone angle for good correlation at hypersonic speeds will be about 20° . Bodies of revolution such as ogives are essentially conical at the nose and decrease in slopes thereafter. Therefore, if the nose of any pointed body is about 20° or less, it should correlate well with this law. For ogives, this means the fineness ratio should be about 3 or more.

Figure 4 presents the pressure-ratio distribution on ogives. The solid lines are the characteristic solutions of Rossow (ref. 4), each of which is for at least two different combinations of M_∞ and l/d within the range shown at the lower right. Although $M_\infty = 12$ was the

highest value of M_∞ used in the calculations, it should be pointed out that this value is not meant to be taken as an upper limit. Also shown are the tangent-cone approximations of Probstein and Bray (ref. 6). For $K \geq 1$, they applied the tangent-cone approximation to Lees' result which is for the case when the shock lies fairly close to the body; and for $K < 1$, that is, when the shock is well removed from the surface of the slender bodies, the tangent-cone approximation is applied to Kármán's result in linearized supersonic flow.

Van Dyke has pointed out in his work on the hypersonic small-disturbance theory (refs. 7 and 8) that the range of applicability of the hypersonic similarity law can be extended to the transonic range by replacing the Mach number term with the Prandtl-Glauert similarity factor $\sqrt{M_\infty^2 - 1}$. The degree to which this correlation is successful is illustrated in figure 5 for cones with semiapex angles of 5° , 10° , 15° , and 20° . In this figure $C_p / \tan^2 \sigma$ is plotted against $\sqrt{M_\infty^2 - 1} \tan \sigma$ for a Mach number range from 1.15 to hypersonic speeds. Each curve is ended when sonic velocity appears on the cone surfaces. The correlation is seen to be excellent.

The correlation for bluff cones as suggested by Newtonian theory is presented in figure 6, where $C_p / \sin^2 \sigma$ is plotted against σ . For the ranges of Mach number and σ shown, a good approximation to the pressure on the surface of a bluff cone is $\frac{C_p}{\sin^2 \sigma} \approx 2.2$.

Shock-expansion theory.- The use of two-dimensional shock-expansion theory to predict the pressures on slender bodies of revolution at zero angle of attack at hypersonic speeds is well known. Eggers and his associates (refs. 1 and 9) have shown that, provided conditions at the nose are known from either conical theory or experiment, the generalized shock-expansion method can be used for slender bodies of revolution at angle of attack.

Figure 7 shows a comparison of the shock-expansion theory with experiment for an ogival nose at an angle of attack of 15° and a free-stream Mach number of 5.05. The symbols show the experimental pressure coefficients along the top, side, and bottom meridians. The theoretical predictions begin with the assumption of conical flow at the nose. The solid curves use the theoretical cone approximation of Savin (ref. 10) as the starting point for the shock-expansion calculations, and the dashed curve uses experimentally determined conditions on the nose cone as the starting point for the calculations. Obviously, a reliable theoretical method is preferable for design work. It is seen that on the bottom meridian, which would be of most interest for loads considerations, the shock-expansion

calculations agree with experiment for both the theoretically and the experimentally determined starting conditions; that is, Savin's theoretical cone results combined with shock-expansion theory will give good design estimates of maximum loads on sharp noses at angle of attack.

Effect of Blunting

In cases where high heat-transfer rates are expected, the use of blunt leading edges and noses is dictated. Figures 8 and 9 present results for both two-dimensional circular cylinders (ref. 11 and 12) and hemispherical-nose bodies of revolution (ref. 13). The results for circular cylinders (fig. 8) would be applicable both to bodies of revolution at high angles of attack and to the leading edges of blunt sweptback wings. Figure 8 is essentially a double correlation of pressure ratios. It shows the manner in which the pressure ratio varies with meridian angle, and it is good for a wide range of sweepback angles. Also note that, as the Mach number increases, the band of experimentally determined pressure ratios converges toward the theoretical curve of Goodwin (ref. 12) shown by the dashed line. Penland (ref. 11) has shown that p_{\max} can be determined on yawed circular cylinders for sweepback angles from 0° to about 75° at $M_\infty = 6.9$ by using the normal component of M_∞ . Thus, the absolute pressure distribution on the windward side of yawed circular cylinders can be obtained.

The results for hemispherical noses in figure 9 show excellent agreement with Newtonian theory. In this figure the pressure-coefficient ratio is plotted against s/r , which is the arc angle in radians. As can be seen, the pressure-coefficient ratio is independent of Mach number. The curve of $C_{p,\max}$ against M_∞ in the upper right of the figure shows that, for values of M_∞ greater than about 4, $C_{p,\max}$ is essentially a constant on the order of 1.8. Thus, with the aid of Newtonian theory, C_p can be closely estimated, and for values of M_∞ above about 4, the C_p distribution will be essentially invariant with M_∞ .

As was mentioned previously, many of the exact flow parameters can be closely approximated with simple expressions in the hypersonic-flow regime. For example, for $\gamma = 1.4$ and $M_\infty \gg 1$, it can be shown that the ratio of free-stream static pressure to stagnation pressure on a blunt-nose body is approximately $0.777/M_\infty^2$. (This ratio is determined

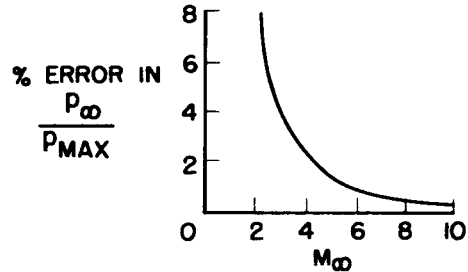
[REDACTED]



in the appendix.) The percentage error in the true value of P_{∞}/P_{MAX} incurred by using the approximation is shown by the sketch. At $M_{\infty} = 3$, the error is only 4 percent and it decreases rapidly thereafter with increasing M_{∞} . It can also be shown that for $M_{\infty} \gg 1$, the ratio of local pressure to maximum pressure is approximately equal to the ratio of local pressure coefficient to maximum pressure coefficient. Consequently, the ratio of the local absolute pressure to the free-stream static pressure is given by

$$\frac{p}{P_{\infty}} \approx \frac{M_{\infty}^2}{0.777} \frac{C_p}{C_{p,MAX}}; \text{ that is, at hyper-}$$

sonic speeds, the absolute pressure at any point on a blunt nose is directly proportional to the square of the Mach number. In particular, for any given altitude, the absolute pressure distribution on a hemispherical nose is given by $\frac{p}{P_{\infty}} = \frac{M_{\infty}^2}{0.777} \cos^2(s/r)$ for $0 \leq s/r \leq 1.3$ radians.



The fact that the experimental pressures deviate from the theoretical pressures beyond about 1.3 radians is due to a combination of entropy, vorticity, and boundary-layer effects, which, of course, Newtonian theory does not include. For the Mach numbers considered in figure 9, the effects are negligible as far as loads are concerned. As the Mach number is increased, however, these effects become increasingly important.

Figure 10 shows how, as a result of entropy gain, the surface pressure at the shoulder varies with Mach number. The model in figure 10 is a two-dimensional flat slab with a sonic-wedge leading edge. The pressures were calculated by simple inviscid shock-expansion theory. It can be seen that, as M_{∞} increases, the shoulder pressure increases to very large values. The pressure on the shoulder of blunt-nose bodies and blunt-leading-edge wings would follow the same trend with Mach number.

Figure 11 presents theoretically and experimentally (ref. 14) determined pressure distributions on a blunt-leading-edge flat plate for a free-stream Mach number of about 7. The theoretically determined pressure distributions were approximated by assuming sonic-wedge leading-edge conditions. Also indicated in the figure is the value of the pressure ratio for no entropy gain and zero vorticity. The assumption that free-stream static pressure exists on the flat plate was acceptable at lower supersonic speeds. At hypersonic speeds, however, the large entropy gain through the normal shock and the large entropy and



vorticity gradients induced in the flow field by the high shock curvature result in the type of pressure distribution shown by the solid curve. This curve was calculated for the inviscid flow at a Mach number of about 7 for the sonic-wedge leading-edge configuration shown at the upper left. The dashed curve is the experimental pressure distribution for the blunt-leading-edge plate shown on the right at one value of Reynolds number. The difference between these two curves is due to the presence of the boundary layer. If the Reynolds number had been lower, the boundary layer would have been thicker and the separation of these two curves would have been greater; the converse being true if the Reynolds number had been higher. It should also be pointed out that, as the Mach number increases, not only does the level of p/p_∞ at the shoulder increase but also the rate of decrease becomes less, so that the entropy and vorticity effects are spread over a greater distance at higher Mach numbers.

Effect of Boundary-Layer Separation

When real fluid effects, including boundary layers, are brought into the picture, the consequences of boundary-layer separation must also be considered. At hypersonic speeds boundary-layer separation is often important, although it can sometimes be neglected.

Figures 12 and 13 illustrate examples of boundary-layer separation which must be considered and boundary-layer separation which may be neglected. Both the body with conical flare ("flared skirt") shown in figure 12 and the body with flapped wing shown in figure 13 were tested at $M_\infty \approx 7$. (See refs. 15 and 16, respectively.) The manner in which the separation point moves rearward along the flared-skirt body with increasing Reynolds number is indicated by the solid line in figure 12. The body-pressure-coefficient distributions for two extreme positions are shown above with corresponding symbols. The importance of knowing whether to design for separated or unseparated flows is obvious. For unseparated flow the skirt pressure is about what would be expected in the absence of viscosity, while the laminar separation region essentially protects the skirt from direct contact with the free stream.

On the other hand, a large portion of the upper surface of the wing with trailing-edge flap (fig. 13) is in a separated-flow region and there is essentially no effect on the upper surface pressure coefficient. Figure 13 shows the flap deflected 16° ; however, the same effects would be true with a negative flap deflection. The loads on the upper surfaces of wings at angle of attack in hypersonic flow are essentially negligible whether separation exists or not; the difference between free-stream pressure and vacuum is so small in comparison with the pressures on the lower surface that, for all practical purposes, the upper surface can be neglected in loads calculations.



The separated flow on the lower surface is confined to a relatively small region. If this separation point were to move forward the lower surface loads would be affected more than shown in figure 13. The magnitude of the loads induced would also depend on the condition of the boundary layer, that is, whether it is laminar or turbulent.

There is as yet not enough knowledge about separation at hypersonic speeds to be able to predict when or where separation will occur for either laminar or turbulent flow.

Aerodynamic Interference

Another field which is relatively unexplored at hypersonic speeds is that of aerodynamic interference and the role that interference plays in altering the expected loads on any component.

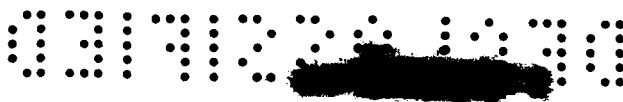
One phase of the interference problem was investigated by building a scale model of a configuration which had previously been tested at $M_\infty = 3.36$. (See refs. 17 and 18.) This model was tested at $M_\infty = 6.85$ in the Langley 11-inch hypersonic tunnel. Some preliminary results are presented herein.

Figures 14 and 15 present the span-load distributions on the wing alone and on the wing in the presence of the body at an angle of attack of 15° for $M_\infty = 3.36$ and $M_\infty = 6.85$, respectively. The overall trends of the results at $M_\infty = 3.36$ are about what would be expected. The results at $M_\infty = 6.85$ show the large localized effect which the thick boundary layer plays in interference between adjacent components. The indicated position of the boundary layer was taken from schlieren pictures at $\alpha = 0^\circ$ on the sharp-nose body. The thickness and condition of the boundary layer at the wing-body juncture at $\alpha = 15^\circ$ is not known. Note also the effect of nose shape on the loadings. The blunt nose decreased the wing loadings. Although the decrement was not appreciable at this Mach number, it is to be expected that the greater losses incurred by a detached shock at higher Mach numbers will more seriously affect the loadings not only on the wing but also on all components within the region of influence of the highly rotational part of the flow field associated with blunt noses.

The shock-expansion theory predicts the loading on the wing alone at $M_\infty = 6.85$ fairly well. The results of the $M_\infty = 3.36$ tests are not a fair test of the adequacy of shock-expansion theory since at $\alpha = 15^\circ$ the leading-edge shock is detached at $M_\infty = 3.36$.

Figure 16 presents the interference loading on the body due to the presence of the wing at an angle of attack of 15° for $M_\infty = 3.36$ on the





sharp-nose body and $M_{\infty} = 6.85$ on the sharp- and blunt-nose bodies. The orientation of the wing and body with respect to the load-distribution curve is as indicated.

Mach number apparently does not play an important role in interference effects in this Mach number range, as evidenced by the fact that the general trends of the interference loading curves on the sharp-nose body at $M_{\infty} = 3.36$ and $M_{\infty} = 6.85$ do not differ widely. The effect of nose shape on body interference loadings is evidenced by the relative displacement of the curves with the square and diamond symbols, and, as already mentioned, the significance of this type of interference will probably increase with increasing M_{∞} . Also of interest is the fact that the maximum interference loading for each of the three curves was 50 to 60 percent of the corresponding body-alone loading.

CONCLUDING REMARKS

This paper has summarized briefly current loads information at hypersonic speeds. Several methods which the designer can employ in estimating the loads on various aircraft components have been discussed. The paper has considered the characteristics of both slender and blunt configurations and the effects of boundary-layer and aerodynamic interference. Many problems still confront the designer - the effect on tail loads of the wing flow field and its associated high-energy wake and the effect of the body flow field and its highly rotational flow for blunt-nose bodies. In addition, the effect on loads at hypersonic speeds of the inert degrees of freedom of the components of the air (molecular vibration, dissociation, and ionization) is essentially unknown.

Langley Aeronautical Laboratory,
National Advisory Committee for Aeronautics,
Langley Field, Va., March 5, 1957.



APPENDIX

PRESSURE RELATION APPROXIMATIONS

The ratio of free-stream static pressure to stagnation pressure for a blunt-nose body can be calculated approximately from the following exact relation (see ref. 19, eq. (100)):

$$\frac{P_{\infty}}{P_{MAX}} = \frac{\left[\frac{2\gamma M_{\infty}^2 - (\gamma - 1)}{\gamma + 1} \right]^{\frac{1}{\gamma-1}}}{\left[\frac{(\gamma + 1) M_{\infty}^2}{2} \right]^{\frac{\gamma}{\gamma-1}}} \tag{1}$$

Since $\frac{\gamma}{\gamma - 1} = \frac{1}{\gamma - 1} + 1$, equation (1) can be written:

$$\frac{P_{\infty}}{P_{MAX}} = \frac{1}{M_{\infty}^2} \frac{\left[\frac{2\gamma}{\gamma + 1} - \frac{(\gamma - 1)}{(\gamma + 1) M_{\infty}^2} \right]^{\frac{1}{\gamma-1}}}{\left[\frac{\gamma + 1}{2} \right]^{\frac{\gamma}{\gamma-1}}} \tag{2}$$

As M_{∞} becomes large, equation (2) is closely approximated by

$$\frac{P_{\infty}}{P_{MAX}} \approx \frac{1}{M_{\infty}^2} \frac{\left[\frac{2\gamma}{\gamma + 1} \right]^{\frac{1}{\gamma-1}}}{\left[\frac{\gamma + 1}{2} \right]^{\frac{\gamma}{\gamma-1}}} \tag{3}$$

For $\gamma = 1.4$, equation (3) becomes

$$\frac{P_{\infty}}{P_{MAX}} \approx \frac{0.777}{M_{\infty}^2} \tag{4}$$



In addition, since

$$C_p = \frac{2}{\gamma M_\infty^2} \left(\frac{p}{p_\infty} - 1 \right)$$

and

$$C_{p,MAX} = \frac{2}{\gamma M_\infty^2} \left(\frac{p_{MAX}}{p_\infty} - 1 \right)$$

the ratio of local surface pressure coefficient to maximum surface pressure coefficient becomes

$$\frac{C_p}{C_{p,MAX}} = \frac{p - p_\infty}{p_{MAX} - p_\infty} = \frac{\frac{p}{p_{MAX}} - \frac{p_\infty}{p_{MAX}}}{1 - \frac{p_\infty}{p_{MAX}}} \quad (5)$$

Rearranging the terms of equation (5) yields

$$\frac{p}{p_{MAX}} = \frac{C_p}{C_{p,MAX}} + \frac{p_\infty}{p_{MAX}} \left(1 - \frac{C_p}{C_{p,MAX}} \right) \quad (6)$$

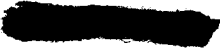
which, with the aid of equation (4), yields for large M_∞

$$\frac{p}{p_{MAX}} \approx \frac{C_p}{C_{p,MAX}} \quad (7)$$





REFERENCES

1. Eggers, A. J., Jr., and Savin, Raymond C.: A Unified Two-Dimensional Approach to the Calculation of Three-Dimensional Hypersonic Flows, With Application to Bodies of Revolution. NACA Rep. 1249, 1955. (Supersedes NACA TN 2811.)
 2. Tsien, Hsue-Shen: Similarity Laws of Hypersonic Flows. Jour. Math. and Phys., vol. XXV, no. 3, Oct. 1946, pp. 247-251.
 3. Ehret, Dorris M., Rossow, Vernon J., and Stevens, Victor I.: An Analysis of the Applicability of the Hypersonic Similarity Law to the Study of Flow About Bodies of Revolution at Zero Angle of Attack. NACA TN 2250, 1950.
 4. Rossow, Vernon J.: Applicability of the Hypersonic Similarity Rule to Pressure Distributions Which Include the Effects of Rotation for Bodies of Revolution at Zero Angle of Attack. NACA TN 2399, 1951.
 5. Lees, Lester: Note on the Hypersonic Similarity Law for an Unyawed Cone. Jour. Aero. Sci. (Readers' Forum), vol. 18, no. 10, Oct. 1951, pp. 700-702.
 6. Probststein, Ronald F., and Bray, Kenneth N. C.: Hypersonic Similarity and the Tangent-Cone Approximation for Unyawed Bodies of Revolution. Jour. Aero. Sci. (Readers' Forum), vol. 22, no. 1, Jan. 1955, pp. 66-68.
 7. Van Dyke, Milton D.: Applications of Hypersonic Small-Disturbance Theory. Jour. Aero. Sci., vol. 21, no. 3, Mar. 1954, pp. 179-186.
 8. Van Dyke, Milton D.: A Study of Hypersonic Small-Disturbance Theory. NACA Rep. 1194, 1954. (Supersedes NACA TN 3173.)
 9. Eggers, A. J., Jr., Savin, Raymond C., and Syvertson, Clarence A.: The Generalized Shock-Expansion Method and Its Application to Bodies Traveling at High Supersonic Air Speeds. Jour. Aero. Sci., vol. 22, no. 4, Apr. 1955, pp. 231-238, 248.
 10. Savin, Raymond C.: Application of the Generalized Shock-Expansion Method to Inclined Bodies of Revolution Traveling at High Supersonic Airspeeds. NACA TN 3349, 1955.
 11. Penland, Jim A.: Aerodynamic Characteristics of a Circular Cylinder at Mach Number 6.86 and Angles of Attack Up to 90°. NACA TN 3861, 1957. (Supersedes NACA RM L54A14.)
- 

12. Goodwin, Glen, Creager, Marcus O., and Winkler, Ernest L.: Investigation of Local Heat-Transfer and Pressure Drag Characteristics of a Yawed Circular Cylinder at Supersonic Speeds. NACA RM A55H31, 1956.
13. Crawford, Davis H., and McCauley, William D.: Investigation of the Laminar Aerodynamic Heat-Transfer Characteristics of a Hemisphere-Cylinder in the Langley 11-Inch Hypersonic Tunnel at a Mach Number of 6.8. NACA TN 3706, 1956.
14. Bertram, Mitchel H.: Viscous and Leading-Edge Thickness Effects on the Pressures on the Surface of a Flat Plate in Hypersonic Flow. Jour. Aero. Sci. (Readers' Forum), vol. 21, no. 6., June 1954, pp. 430-431.
15. Becker, John V., and Korycinski, Peter F.: Heat Transfer and Pressure Distribution at a Mach Number of 6.8 on Bodies With Conical Flares and Extensive Flow Separation. NACA RM L56F22, 1956.
16. Ridyard, Herbert W., and Fetterman, David E., Jr.: Aerodynamic Characteristics of a 6-Percent-Thick Symmetrical Circular-Arc Airfoil Having a 30-Percent-Chord Trailing-Edge Flap at a Mach Number of 6.9. NACA RM L56B24, 1956.
17. Hill, William A., and Kaattari, George E.: Force and Pressure-Distribution Investigation to High Angles of Attack on All-Movable Triangular and Rectangular Wings in Combination With a Body at Supersonic Speeds. NACA RM A56C12, 1956.
18. Kaattari, G. E.: Pressure Distributions on Triangular and Rectangular Wings to High Angles of Attack - Mach Numbers 2.46 and 3.36. NACA RM A54J12, 1955.
19. Ames Research Staff: Equations, Tables, and Charts for Compressible Flow. NACA Rep. 1135, 1953. (Supersedes NACA TN 1428.)



TENDENCY TOWARD TWO-DIMENSIONALITY OF FLOW AT HYPERSONIC SPEEDS

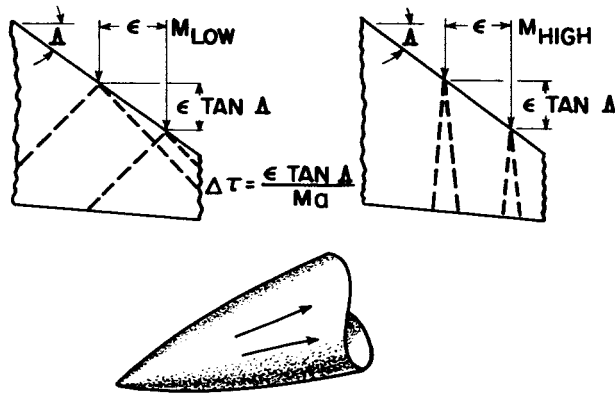


Figure 1

PHYSICAL CONCEPT FOR HYPERSONIC SIMILARITY LAW

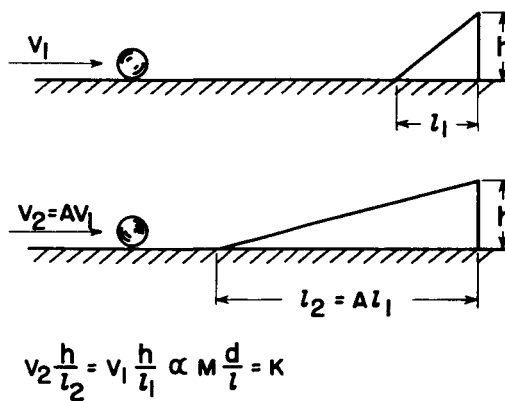
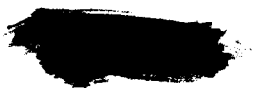


Figure 2





RANGE OF APPLICABILITY OF HYPERSONIC SIMILARITY LAW ($K=M_\infty \frac{d}{l}$) FOR CONES

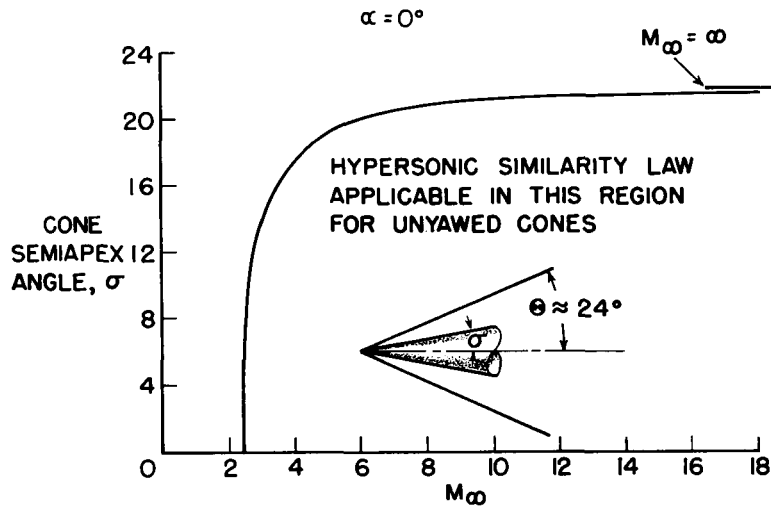


Figure 3

APPLICABILITY OF HYPERSONIC SIMILARITY LAW TO SLENDER BODIES

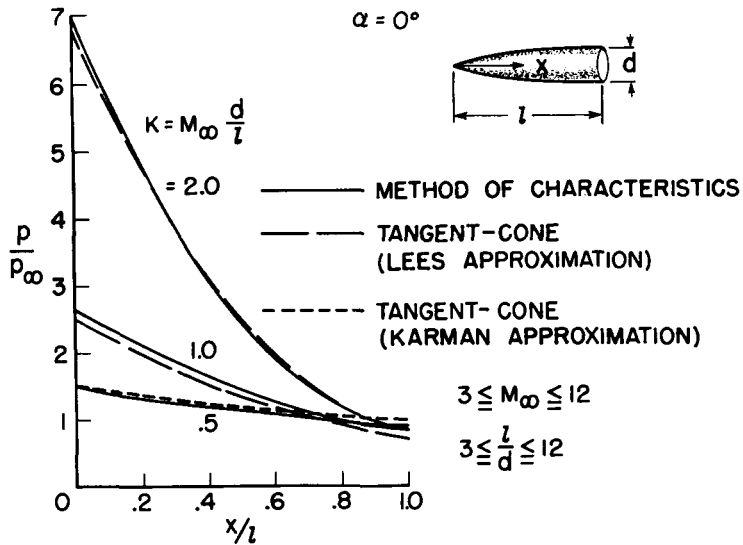


Figure 4





CORRELATION OF THEORETICAL PRESSURE COEFFICIENTS
ON SLENDER UNYAWED CONES
COMBINED SUPERSONIC-HYPERSONIC SIMILARITY RULE

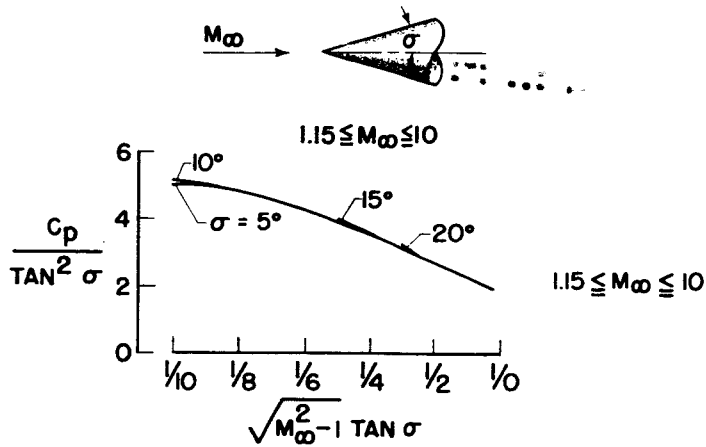


Figure 5

CORRELATION OF THEORETICAL PRESSURE COEFFICIENTS
ON BLUFF UNYAWED CONES

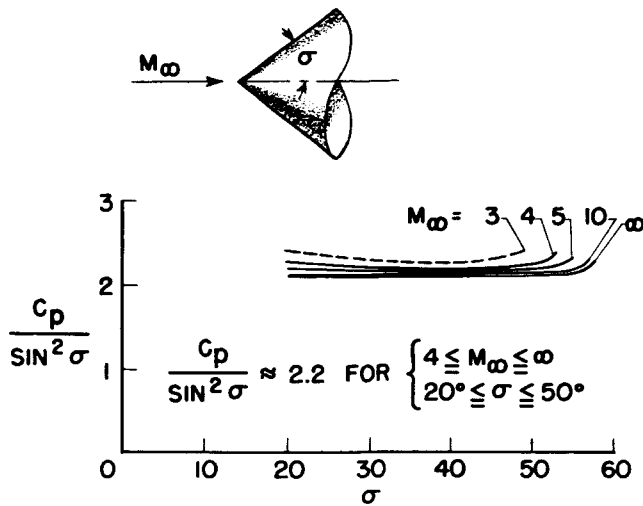


Figure 6





PREDICTION OF PRESSURE DISTRIBUTION ON OGIVE AT
 ANGLE OF ATTACK
 GENERALIZED SHOCK-EXPANSION METHOD; $M_\infty = 5.05$

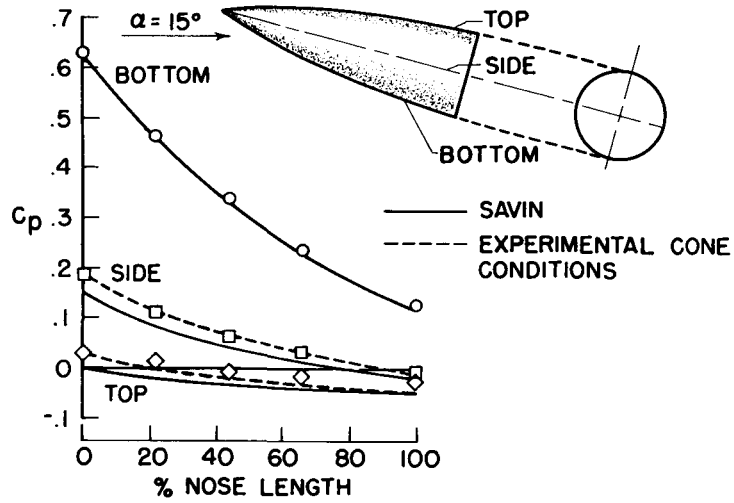


Figure 7

INVARIANCE OF CYLINDER PRESSURE RATIO WITH
 MACH NUMBER AND SWEEP ANGLE

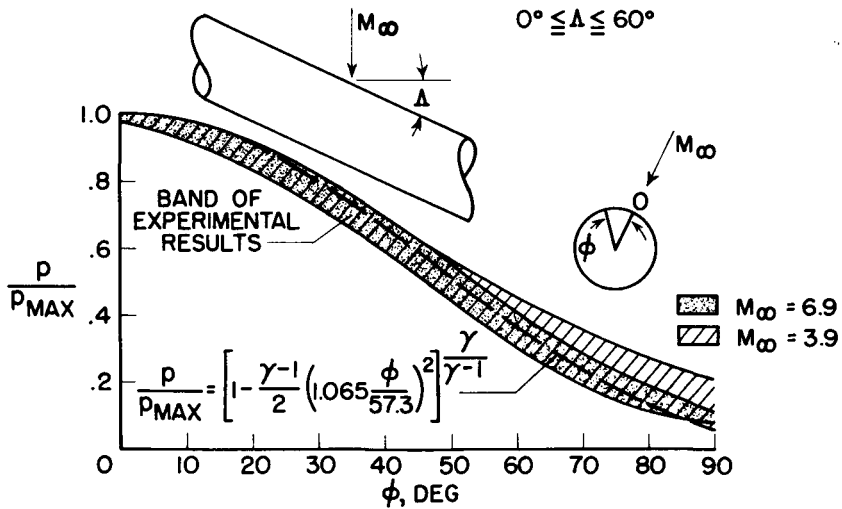


Figure 8





INVARIANCE OF PRESSURE-COEFFICIENT RATIO WITH MACH NUMBER FOR HEMISPHERICAL NOSES

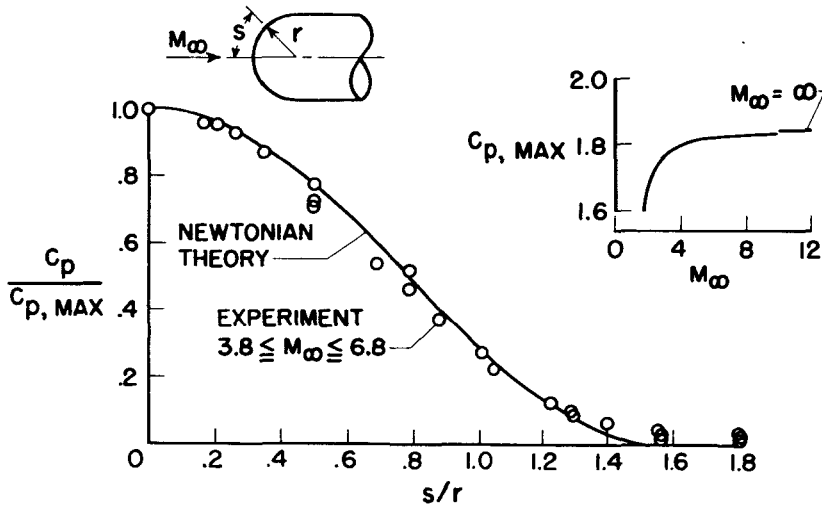


Figure 9

EFFECT OF ENTROPY ON SHOULDER PRESSURE OF SONIC-WEDGE FLAT PLATE

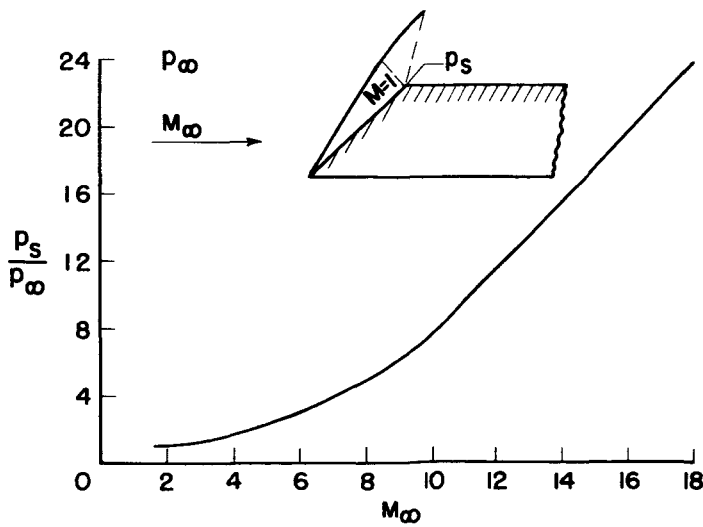


Figure 10





EFFECT OF BOUNDARY LAYER AND ENTROPY ON
FLAT-PLATE PRESSURES

$M_\infty \approx 7; \gamma = 1.4$

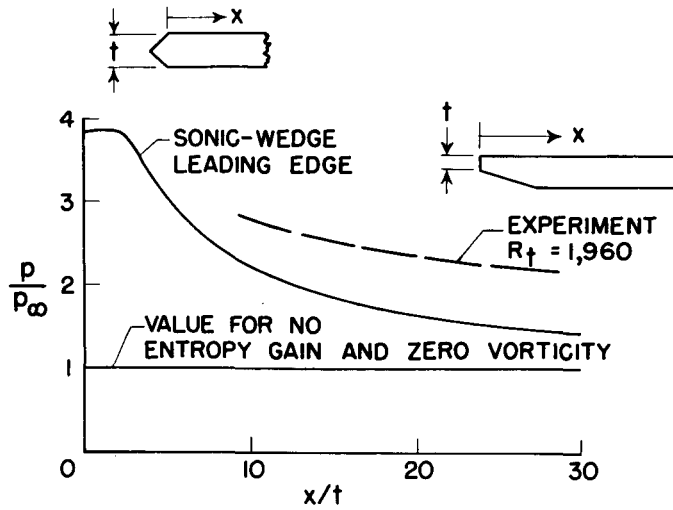


Figure 11

EFFECT OF SEPARATION ON PRESSURE DISTRIBUTION
ON BODY OF REVOLUTION

$M_\infty \approx 7; \alpha = 0^\circ$

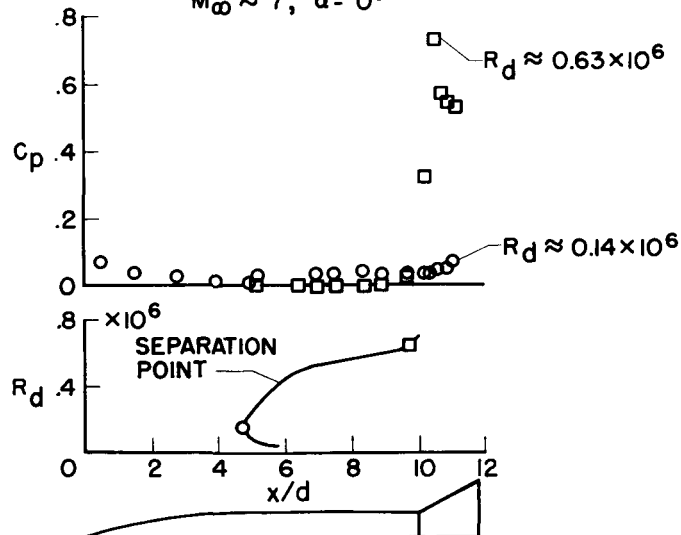
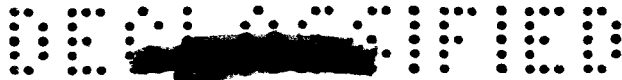


Figure 12





EFFECT OF SEPARATION ON PRESSURES ON TWO-DIMENSIONAL WING FLAP

$\alpha = 16^\circ$; $\delta = 16^\circ$; $M_\infty \approx 7$; $R = 1.65 \times 10^6$

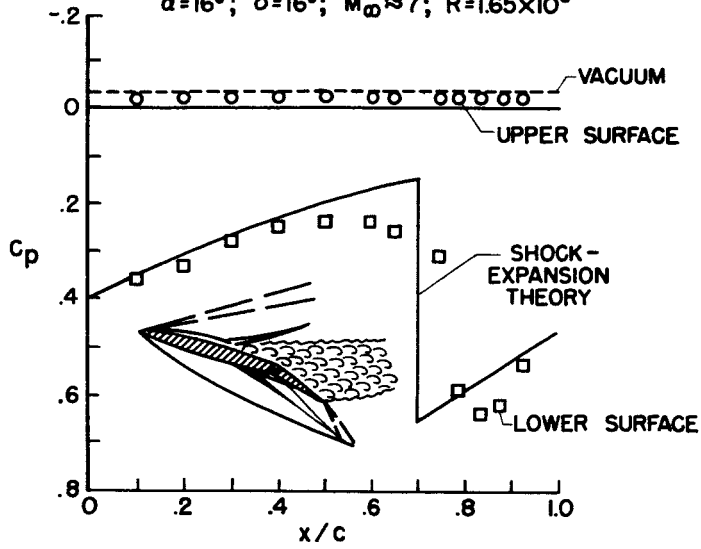


Figure 13

INTERFERENCE ON WING LOAD DISTRIBUTION AT $\alpha = 15^\circ$

$M_\infty = 3.36$

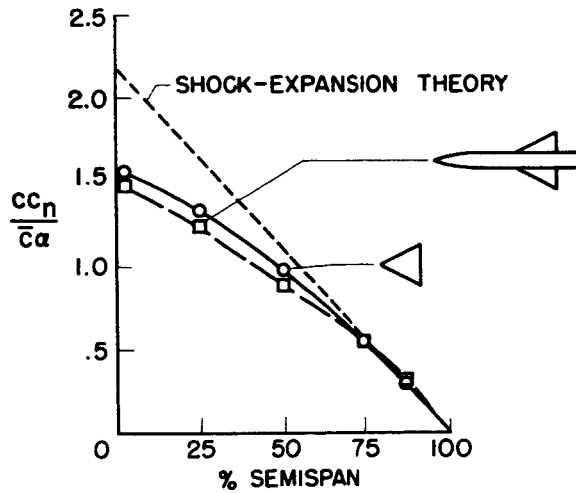


Figure 14





INTERFERENCE ON WING LOAD DISTRIBUTION AT $\alpha=15^\circ$
 $M_\infty=6.85$

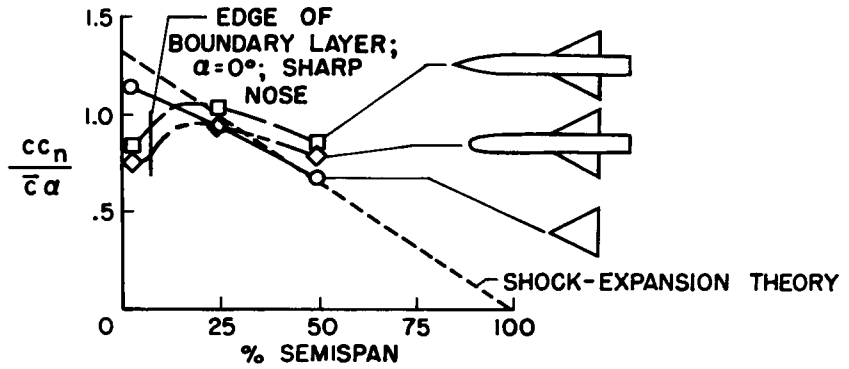


Figure 15

INTERFERENCE ON BODY LOAD DISTRIBUTION DUE TO WING
 $\alpha=15^\circ$

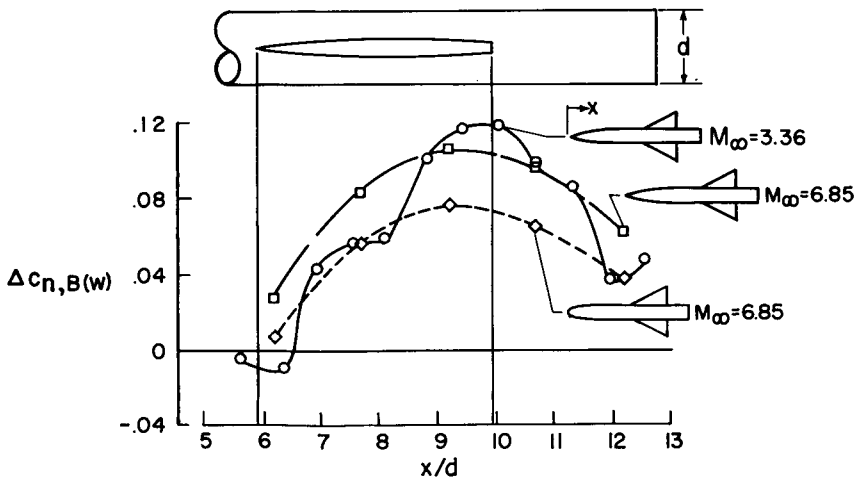


Figure 16

